Assessing Cardiac Tissue Function via Action Potential Wave Imaging Using Cardiac Displacement Data

Niels F. Otani, Dylan Dang, Shusil Dangi, Mike Stees, Suzanne M. Shontz and Cristian A. Linte

1 Background

The ability to visualize action potentials deep within the walls of the heart has important applications. It enables the identification of regions of electrically and mechanically compromised tissue that can mark the location(s) of infarcted and ischemic myocardial tissue, and also permits the visualization of normal and abnormal action potential wave propagation patterns for use in both clinical and cardiac research settings. Recently, we have been investigating the possibility of using 4-D mechanical deformation data, obtained either from MRI or ultrasound images, to reverse-calculate these action potential patterns [4, 5, 2]. This idea has also been studied by Konofagou *et al.* [6], who used mixed time and space second derivatives in the displacement fields to identify the location of action potentials. While this mixed-derivative method should be effective for spatially one-dimensional action potentials, it is less effective when propagation of the waves is fundamentally three-dimensional.

To reconstruct three-dimensional propagation, we have demonstrated that solving the full, force-balance equation in three spatial dimensions for the active stresses

Niels F. Otani
Rochester Institute of Technology, Rochester, NY 14623, U.S.A., e-mail: nfosma@rit.edu

Dylan Dang
Rochester Institute of Technology, Rochester, NY 14623, U.S.A., e-mail: dnd6444@rit.edu

Shusil Dangi
Rochester Institute of Technology, Rochester, NY 14623, U.S.A., e-mail: sxd7257@rit.edu

Michael Stees
University of Kansas, Lawrence, KS 66045, U.S.A., e-mail: mstees@ku.edu

Suzanne M. Shontz
University of Kansas, Lawrence, KS 66045, U.S.A., e-mail: shontz@ku.edu

Cristian A. Linte
Rochester Institute of Technology, Rochester, NY 14623, U.S.A., e-mail: clinte@mail.rit.edu

induced by the action potentials, using observed deformations as input, is mathematically a viable method. We can then consider the calculated active stress field to be a surrogate for the pattern of action potentials, since the action potentials essentially trigger the generation of active stresses. While the ability to reconstruct imposed stresses from observed strains is, in general, an underdetermined problem, for the case of the heart it is overdetermined, because active stresses are known to be oriented exclusively along the myocardial fiber direction, which greatly reduces the number of unknowns [4, 5].

In previous work, we took advantage of this constraint to show that active stresses, and therefore the action potential locations, can be reasonably well determined in simple geometries in the presence of both noise in the displacement fields and uncertainty in the fiber orientations [4]. For the study presented here, we show that this same method can also identify the locations of compromised tissue through the latter's modified or lack of ability to contract in the presence of an action potential. Thus, our method could potentially lead to new, non-invasive cardiac imaging-based diagnostic methods that could help to identify regions affected by cardiac disease that leads to impaired contractile function.

2 The Basic Method

Our method consists of solving the three-dimensional force-balance equation together with the assumption of tissue incompressibility. For our preliminary tests of the properties and effectiveness of this method, we employed the linearized version of these equations, namely,

$$\frac{\partial}{\partial x_N}\left[\frac{1}{2}\frac{\partial T_{NM}}{\partial E_{PQ}}(0)\left(\frac{\partial \delta x_P}{\partial x_Q}+\frac{\partial \delta x_Q}{\partial x_P}\right)+T_{NM}^{active}-p\delta_{NM}\right]=0 \tag{1}$$

and

$$\frac{\partial \delta x_M}{\partial x_M}=0 \tag{2}$$

Here $T_{NM}(E)$ is the passive second Piola-Kirchhoff stress tensor, which depends on the strain tensor E_{PQ}, δx_P is the tissue displacement in the x_P direction, p is the local hydrostatic pressure, δ_{NM} is 1 when $N=M$ and 0 otherwise, and T_{MN}^{active} is the stress tensor due to the action-potential-induced force generated parallel to the orientation of the myocardial fibers. Sums over repeated indices are implicit. The stiffness tensor, $(\partial T_{NM}/\partial E_{PQ})(0)$ was defined from the model of Nash and Hunter [3].

We first solved the equations in a synthetic tissue sample of isotropic resolution along the three spatial directions (i.e., a cubic synthetic tissue sample) using stress-free boundary conditions. We defined the myocardial fiber system in a realistic way, with the fiber directions rotating smoothly about the vertical (y) axis from the bottom to the top of the synthetic tissue sample.

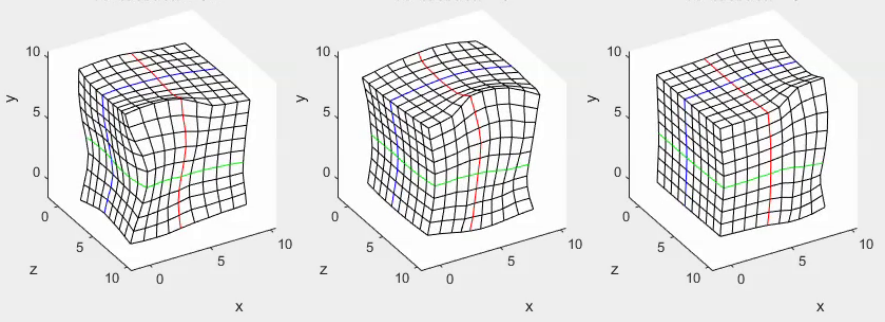

Fig. 1 Deformations calculated from the forward model at three different times in response to a plane wave pattern of active stresses propagating in the positive x-direction.

We used these governing equations to solve the forward problem in which we quantified the tissue deformation (the δx_P's) in response to the prescribed active stress (T_{MN}^{active}'s). The forward model enabled us to generate the tissue deformation data (i.e., the displacement field) needed as input in the inverse problem, which is the ultimate objective of this work. To solve the inverse problem, we used the same governing equations, but solved for the active stress using the displacement field as input. The equations were solved using a low-order finite element method based on the rectangular isotropic mesh of the synthetic cubic tissue sample introduced earlier.

3 Numerical Evaluation and Noise Sensitivity Analysis

Our test case was to launch a plane wave "action potential" from the left side of the system in Fig. 1, which was represented as a region of nonzero active stress. Specifically, at each point within the moving plane wave region, we defined the active stress to be $T^{active} = T_0 \hat{x}_\alpha \hat{x}_\alpha$, where T_0 is a nonzero constant, and $\hat{x}_\alpha$ is a unit vector aligned along the local fiber direction. The active stress tensor was defined to be zero everywhere outside the plane wave region.

The primary scope of this study was to faithfully reconstruct the active stresses from displacement data as a means to detect and assess the extent of possible ischemic or infarcted regions. Accordingly, we defined a few cubic regions of varying sizes within the synthetic tissue sample and prescribed to them zero active stress as the action potential plane wave passed through them, thereby mimicking non-contractile (i.e., no active stress generating) regions. We then ran the forward model and computed the tissue displacement field shown in Fig. 1 in response to the prescribed active-stress plane wave. Next, we added noise (0 mean, 1% standard deviation) to this displacement field, to represent the effects of errors and uncertainty that would typically be present in the measured data. Finally, this "noisy displacement data" was used as input into our inverse model.

The accuracy of the inverse algorithm, and its robustness in the presence of noise, was assessed by comparing the active stress distribution reconstructed from the noisy displacement data to the originally prescribed active stress distribution, and by identifying the effectiveness of the generated active stress maps in revealing the synthetic regions that mimicked compromised contractile function.

Cross-sections of the calculated active stresses at different times are shown in Fig. 2. We observed that any regions exhibiting poor contractile function (bounded by dotted lines) that were 2x2x2 pixels or larger in size were clearly visible as lighter-colored (lower active stress) regions as the action potential (inside the dashed lines) passed through them. The presence of the poorly contractile regions was even more apparent when the plots were viewed in sequence, as a movie.

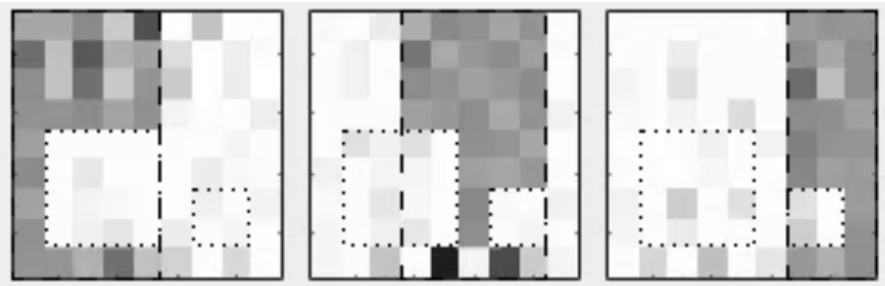

Fig. 2 Grayscale plot of the active stress along the local fiber direction in a cross-section of the system showing at three different times. The actives stresses were calculated by the inverse model using as input the deformations shown in Fig. 1 to which was added 1% noise. The dashed line shows the boundaries of the plane wave of active stresses; the dotted line shows the boundary of any cubic "dead" region through which the cross-section passed.

4 Integration of Realistic Cardiac Geometries and Tetrahedral Computational Meshes

In preparation for applying this method to actual cardiac data, we have been developing methods for individualized segmentation of the cardiac anatomy from diagnostic, clinical-quality cardiac MRI images, which we can then use to generate static and dynamic patient-specific myocardial models to be subsequently employed for computing the active stresses.

Specifically, we developed a framework for left ventricle (LV) segmentation from cardiac cine-MRI. First, we segment the LV blood pool using iterative graph cuts, and subsequently use this information to segment the myocardium. We formulate the segmentation procedure as an energy minimization problem in a graph subject to the shape prior obtained by label propagation from an average atlas using affine registration. The proposed framework has been validated on 30 patient car-

diac cine-MRI datasets available through the Statistical Atlases and Computational Models of the Heart (STACOM) Left Ventricle (LV) segmentation challenge using traditional segmentation assessment metrics, such as Dice index, Jaccard index, sensitivity, specificity, positive predictive value (PPV), and negative predictive value (NPV), and yielded fast, robust, and accurate segmentation results. Lastly, the proposed algorithm was implemented in Python and required 45 seconds on average to segment the blood pool and myocardium from cine MRI volumes on an Intel Xenon 3.60 GHz 32GB RAM PC [1].

A similar approach has been implemented for the segmentation of the right ventricle from cardiac cine MR images [10]. While the right ventricle is not as extensively studies as the left ventricle, there are nevertheless many unanswered questions with respect to assessing and understanding its shape and geometry. **Fig. 3** shows the typical three orthogonal views through a cine cardiac MRI dataset, along with the segmentation of the right ventricle on a slice-by-slice basis, as well as a 3D reconstruction of a surface mesh.

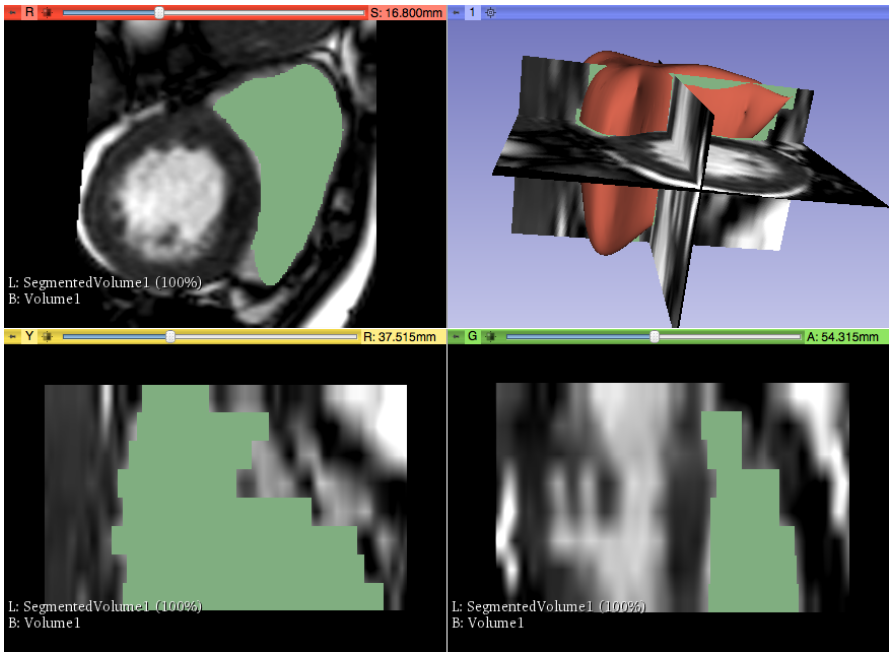

Fig. 3 Axial, Sagittal, Coronal, and the 3D model (counter-clockwise from top left) of the segmented RV blood pool overlayed onto the MRI image.

Moreover, **Fig. 4** shows the assessment of the segmented and reconstructed right ventricle surface against the geometry of the same chamber reconstructed based on the manual user's ground truth segmentation [10]. In essence, we computed the signed distance between the surface generated using automated segmentation and

the surface generated from the manually segmented data, and assigned the signed distance value as a scalar to each mesh node of the surface model, then interpolated across all all nodes and elements to obtain the signed distance error map shown in **Fig. 4**.

This approach constitutes a means to evaluate the fidelity of the automatically generated surface model both quantitatively, according to the mesh-to-mesh signed distance, as well as qualitatively, by ensuring that the overall fidelity of the segmented cardiac chamber has not been compromised by the automated segmentation. The underlying assumption is that the surface model generated from the manually segmented data serves as the accepted ground truth model.

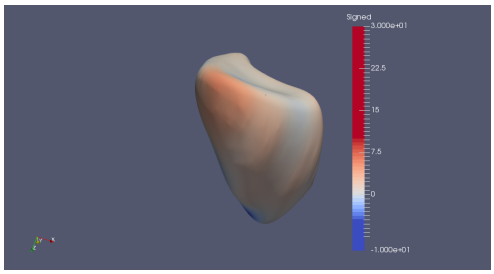

Fig. 4 Signed distance error between the segmented right ventricle blood pool and the corresponding gold standard manual segmentation overlayed onto the 3D model of the latter.

The 3D anatomical models shown in Figs. 3 and 4 were obtained by generating an iso-surface along the segmentation mask using the well-known marching cubes algorithm [7]. After generating the surface mesh using marching cubes, we used MeshLab [8] to apply several post-processing transformations. Essentially, the resulting surface was then decimated to significantly reduce the number of surface triangles, however without compromising the fidelity of the surface.

The transformations were executed in two phases. The purpose of the first phase was to eliminate duplicate nodes in the input surface mesh. Following this, the second phase emphasized the elimination of low quality triangles from the surface. This elimination was performed using the following three techniques: (1) edge collapses, (2) Laplacian smoothing, and (3) edge flips. These operations attempt to improve the mesh quality by changing the mesh topology and moving mesh nodes.

In Fig. 5, we show the initial surface mesh generated by marching cubes, the improved mesh using the process we described above, and a rotated view of the original and improved mesh, respectively. In addition, the triangle color in Fig. 5 corresponds to the quality of the element as measured by the ratio of the inradius to the circumradius. The color blue indicates element quality in the range $(0.65-1]$ (with dark blue being the highest quality and light blue being the lowest quality); green indicates element quality in the range $(0.35-0.65]$ (with dark green being the highest quality and light green being the lowest quality); yellow and red indicate element quality in the range $(0-0.35]$ (with yellow being the highest quality and red being the lowest quality).

By comparing the two meshes in Figs. 5(a) and 5(c), we can see significantly more blue elements in the improved mesh. This indicates that our elimination pro-

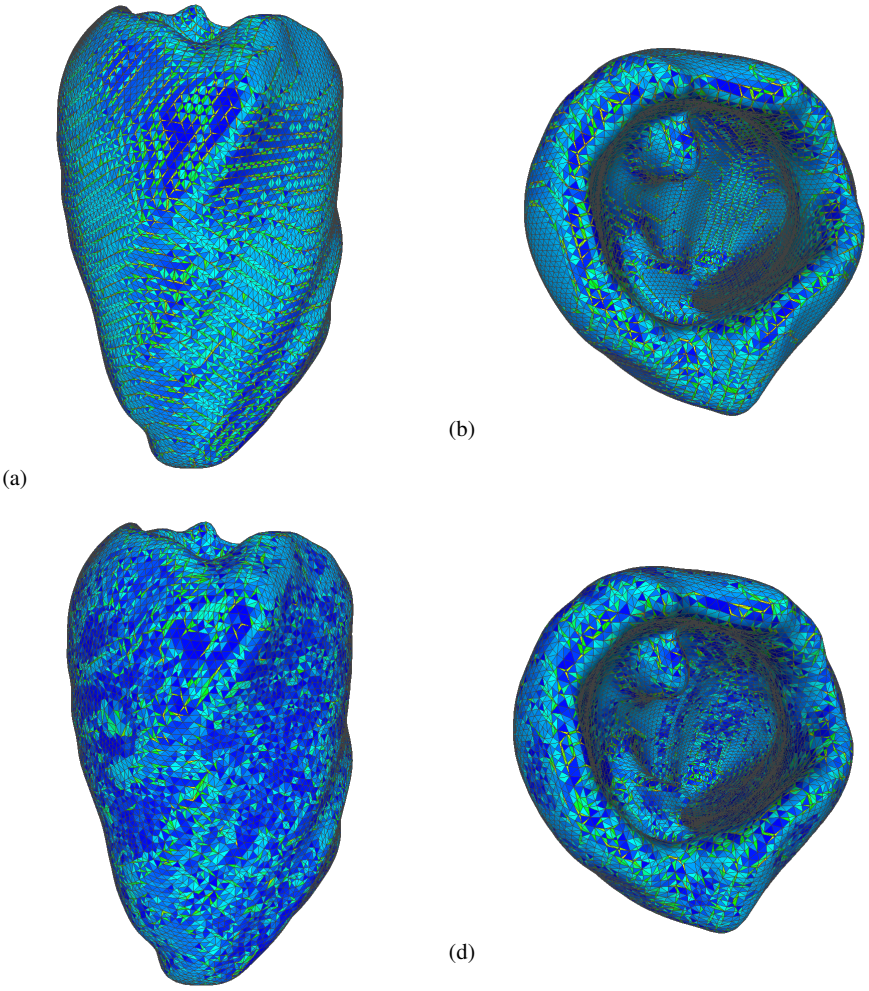

Fig. 5 The surface meshes: (a) generated by marching cubes, (b) rotated view of (a), (c) after applying the improvement transformations, and (d) rotated view of (c).

cess did in fact improve the quality of the surface mesh.

The improved surface mesh was then used as input to the Delaunay-based tetrahedral mesh generator, TetGen [9]. To enforce the creation of a quality volume mesh, we used the quality flag in TetGen with a value of 1.2. This value sets the maximum allowable radius to edge ratio to 1.2. To assess the quality of the tetrahedral mesh, we used the aspect ratio metric. The ideal value of the aspect ratio is 1.0. In Fig. 7, we show the number of elements in each range of aspect ratio values. In Fig. 6

we show a cut-away view of the tetrahedral volume mesh constructed with TetGen. The cyan elements correspond to triangles on the surface mesh, while the magenta elements correspond to tetrahedra in the volume mesh. An important detail to note is that the volume mesh conforms to the surface mesh.

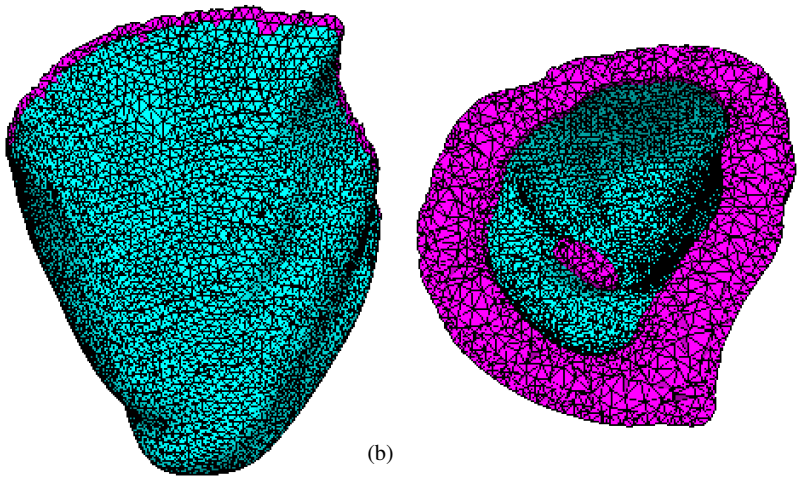

(a) (b)

Fig. 6 A cut-away view of the tetrahedral volume mesh: (a) in the upright orientation, and (b) in the rotated orientation.

5 Summary, Conclusion and Future Work

Previously, we demonstrated that it is possible to reconstruct the active stresses created by propagating action potentials in the myocardium by reverse-calculating them from the mechanical deformations they produce. These active stresses can often play the role of surrogates for the action potentials. Therefore, a method that helps quantify the active stresses may serve as the basis for a new visualization technique that allows us to see patterns of action potential propagation deep within the heart, using MRI or ultrasound images as input.

In this study, we demonstrate that the reconstructed active stresses can also be used to identify functionally compromised regions within the heart, such as those dominated by ischemic or infarcted tissue. We also show again, by means of a numerical simulation involving a synthetic tissue sample of simplified geometry, that our inverse method is able to reconstruct active stresses from tissue deformation data.

Lastly, in preparation for the next step in our study, we have developed new segmentation techniques and generated tetrahedral volume meshes of the myocardium

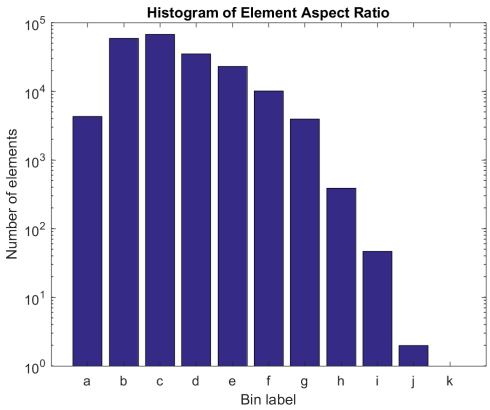

Fig. 7 A histogram of element quality as measured by aspect ratio. The y-axis is displayed on a logarithmic scale. See the legend below which pairs each x-axis label with the corresponding range of aspect ratio values.

label	range
a	$[1, 1.5)$
b	$[1.5, 2)$
c	$[2, 2.5)$
d	$[2.5, 3)$
e	$[3, 4)$
f	$[4, 6)$
g	$[6, 10)$
h	$[10, 15)$
i	$[15, 25)$
j	$[25, 50)$
k	$[50, 100)$

which will allow us to test these ideas in realistic, individualized heart geometries using meshes which faithfully model the geometry. In the future, we will develop dynamic meshing algorithms in order to simulate cardiac deformations on deforming meshes.

6 Acknowledgment

The techniques presented here were implemented and tested on cardiac cine MRI image datasets made available through the through the Statistical Atlases and Computational Models of the Heart (STACOM) cardiac segmentation challenge (http://www.cardiacatlas.org/challenges/lv-segmentation-challenge/).

References

1. Dangi S, Cahill ND, Linte CA (2017) Integrating atlas and graph cut methods for left ventricle segmentation from cardiac cine MRI. Lect Notes Comput Sci Statistical Atlases and Computational Models of the Heart (STACOM) 10124:76-86.
2. Linte CA, Wierzbicki M, Peters TM, Samani A (2008) Towards a biomechanics-based technique for assessing myocardial contractility: An inverse problem approach. Comput Methods Biomech Biomed Engin 11(3):243-255.
3. Nash MP, Hunter PJ (2000) Computational mechanics of the heart. J Elasticity 61:113-141.
4. Otani NF, Luther S, Singh R, Gilmour RF Jr (2010) Transmural ultrasound-based visualization of patterns of action potential wave propagation in cardiac tissue. Ann Biomed Eng 38:3112-3123.
5. Otani NF, Luther S, Singh R, Gilmour RF Jr (2014) Methods and systems for functional imaging of cardiac tissue. U.S. Patent No. 8,666,138.
6. Provost J, Lee WN, Fujikura K, Konofagou EE (2010) Electromagnetic wave imaging of normal and ischemic hearts in vivo. IEEE Trans Med Imaging 29:625-635.
7. Lorensen, WE, Cline, HE (1987) Marching cubes: A high resolution 3D surface construction algorithm. ACM SIGGRAPH Computer Graphics.
8. Cignoni, P, Callieri, M, Corsini, M, Dellepiane, M, Ganovelli, F, Ranzuglia, G (2008) MeshLab: an Open-Source Mesh Processing Tool. Eurographics Italian Chapter Conference.
9. Si, H. (2015) TetGen, a Delaunay-based quality tetrahedral mesh generator. ACM Transactions on Mathematical Software.
10. Dangi S, Linte CA (2017) Using Atlas Prior with Graph Cut Methods for Right Ventricle Segmentation from Cardiac MRI. Lect Notes Comput Sci - Functional Imaging and Modeling of the Heart. 10263:83-94.